Journal of Applied Mechanics and Technical Physics, Vol. 37, No. 5, 1996

EVOLUTION OF SINGULAR POINTS AND INTERFACES SEPARATING THE DOMAIN OF RESIDENCE OF THESE POINTS FROM THE FLUID

N. A. Inogamov[1] and A. Yu. Dem'yanov[2]

UDC 532.5

Hydromechanical theories are by far based mainly on the concepts of vortices. Studying vortices assumes studying their generation and evolution. Since the circulation in a homogeneous fluid is preserved, vorticity generation in the absence of solid boundaries is possible only at density discontinuities. Therefore, an analysis of the dynamics of such discontinuities, which are also called contact surfaces or interfaces, is of fundamental importance.

These problems are developed in the present paper. The development is based on the concepts of singularities of the velocity potential, which go back to S. A. Chaplygin. These singularities are in a sense virtual, because they are outside the region occupied by the fluid. In this case, stationary solutions and singularities in a steady state are usually dealt with. Here we consider the movements of singularities and the nonstationary effects. The hypothesis that the singularity trajectory can meet a fluid boundary is discussed. At the moment of contact with the fluid, the singularity would be transformed from virtual into real. The results obtained are based on high-order expansions of the classical boundary conditions at the boundary surface and direct numerical modeling of fluid flow with density discontinuities. Analytical expansions are performed for $\mu = 0$ (μ is the density ratio), when one fluid is contiguous with another fluid of infinitely small density (vacuum). They can be used until the appearance of a singularity. When the two conditions are satisfied, the function $y = \eta(x,t)$, which gives the boundary, remains a single-valued function of x. At the same time, numerical calculations were performed for $\mu \neq 0$, since, unfortunately, the numerical methods used cannot be applied for $\mu = 0$. In this case, a mushroom-shaped bluntness originates in the lower part of the jet and the Kelvin–Helmholtz instability can appear at the jet boundary. These effects are undesirable from the point of view of the aims of this paper. To weaken them, calculations were performed for $\mu \ll 1$.

1. Basic Equations. The dynamics of a nonhomogeneous incompressible fluid in the nonstationary case is described by the equations

$$D_t\mathbf{v} + (\nabla p)/\rho - \mathbf{g} = 0, \quad (\nabla \cdot \mathbf{v}) = 0, \quad D_t\rho = 0, \quad D_t = \partial_t + (\mathbf{v} \cdot \nabla), \tag{1.1}$$

where $\mathbf{v} = \{u, v\}$, ρ, p, and $\mathbf{g}$ are the velocity, density, pressure, and the acceleration of gravity, respectively. The last equation in this system describes the transfer of density inhomogeneities. The case of an incompressible fluid is studied below analytically and numerically. In addition, the compressibility effect of the fluid is analyzed numerically for small Mach numbers. The corresponding equations have the form

$$D_t\mathbf{v}\ldots, \quad \rho_t + (\nabla \cdot \rho\mathbf{v}) = 0, \quad D_t(\varepsilon + \mathbf{v}^2/2) + (\nabla \cdot p\mathbf{v})/\rho - (\mathbf{g} \cdot \mathbf{v}) = 0, \quad p = (\gamma - 1)\rho\varepsilon. \tag{1.2}$$

Here the first equation $D_t\mathbf{v} + \ldots$, which is related to the momentum, coincides with the first equation of system (1.1); ε is the internal energy per unit mass; and γ is an adiabatic exponent.

[1]Landau Institute of Theoretical Physics, Russian Academy of Sciences, Chernogolovka 142432. [2]Moscow Physical-Technical Institute, Dolgoprudnyi 141700. Translated from Prikladnaya Mekhanika i Tekhnicheskaya Fizika, Vol. 37, No. 5, pp. 93–105, September–October, 1996. Original article submitted May 10, 1995; revision submitted June 26, 1995.

 0021-8944/96/3705-0692 $15.00 © 1997 Plenum Publishing Corporation

The paper is concerned with the evolution of density discontinuities. The ρ distribution has a discontinuity at the boundary surface $\eta(x,t)$. At the initial moment, $\rho = \rho_1$ for $y > \eta$ and $\rho = \rho_2$ for $y < \eta$. We assume that $\mu = \rho_2/\rho_1$. The p distribution at $t = 0$ is found from the equation of hydrostatics. In the regions of $y > \eta$ and $y < \eta$, the motion is vortex-free (rot v = 0). Systems (1.1) and (1.2) are integrated by direct numerical difference methods on a grid covering the rectangular computation domain. An analytical theory is constructed in terms of the scalar velocity potential φ ($\mathbf{v} = \nabla\varphi$). In this case, as is known, system (1.1) reduces to the boundary-value problem. The potential obeys the equation $\Delta\varphi = 0$ for $y > \eta$ and $y < \eta$. In addition, two boundary conditions are satisfied. We restrict ourselves to $\rho_2 = 0$ and $\mu = 0$. The classical [1–4] kinematic and dynamic boundary conditions

$$(-\eta_t + \varphi_y - \eta_x\varphi_x)\Big|_{y=\eta} = 0, \quad (-\varphi_t - v^2/2 + gy)\Big|_{y=\eta} = 0 \tag{1.3}$$

follow from the equation of surface advection and the Bernoulli equation, respectively.

The problem of describing the behavior of density discontinuities arises in a wide spectrum of applications, for example, in connection with the Richtmyer–Meshkov [5–9] and Rayleigh–Taylor [9–16] instabilities.

2. Analytical Results. Let the perturbations be periodic. We expand η and φ into harmonic series

$$\eta(x,t) = \sum_{n=1}^{N+1} s_n(t)\cos(nx), \quad \varphi(x,y,t) = \sum_{n=1}^{N} a_n(t)\cos(nx)\exp(-ny)/n, \tag{2.1}$$

and η into a power series

$$\eta(x,t) = \sum_{n=0}^{N} \eta_n(t)x^{2n}. \tag{2.2}$$

The coefficients s_n and η_n are related to each other by simple linear relationships. Let us move over to an accompanying system of coordinates related to the point ($x = 0$, $y = \eta_0$) at the boundary η. The transformation $x, y \to x, Y$ has the form $Y = y - \eta_0$. The series for φ (2.1) in this system takes the form

$$\Phi(x,Y,t) = \sum_{n=1}^{N} A_n(t)\cos(nx)\exp(-nY)/n - \dot\eta_0(t)\,Y, \quad A_n = a_n\exp(-n\eta_0). \tag{2.3}$$

We substitute series (2.2) and (2.3) into boundary conditions (1.3). After cumbersome calculations [17], which will not be shown here in detail, we obtain a system of ordinary differential equations that determine the evolution of the unknown functions $A_n(t)$ and $\eta_n(t)$:

$$-\dot M_1/2 + \dot M_0\eta_1 = -M_1^2/2 + g\eta_1; \tag{2.4}$$

$$\dot M_3/24 - \dot M_2\eta_1/2 + \dot M_1\eta_1^2/2 + \dot M_0\eta_2 = -M_2^2/8 + M_1M_3/6 - M_1M_2\eta_1/2 - M_1^2\eta_1^2/2 + g\eta_2; \tag{2.5}$$

$$-\dot M_5/720 + \ldots + \dot M_1\eta_1\eta_2 + \dot M_0\eta_3 = -M_3^2/72 + M_2M_4/48 - \ldots - M_1^2\eta_1\eta_2 + g\eta_3; \tag{2.6}$$

$$\dot M_7/40320 - \ldots + \dot M_1\eta_1\eta_3 + \dot M_0\eta_4 = -M_4^2/1152 + M_3M_5/720 - \ldots - M_1^2\eta_1\eta_3 + g\eta_4; \tag{2.7}$$

$$-\dot M_9/3628800 + \ldots + \dot M_1\eta_1\eta_4 + \dot M_0\eta_5 = -M_5^2/28800 + M_4M_6/17280 - \ldots - M_1^2\eta_1\eta_4 + g\eta_5; \tag{2.8}$$

$$\dot M_{11}/479001600 - \ldots + \dot M_1\eta_1\eta_5 + \dot M_0\eta_6 = -M_6^2/1036800 + M_5M_7/604800 - \ldots + g\eta_6; \tag{2.9}$$

$$\dot\eta_1 = -M_2/2 + 3M_1\eta_1; \tag{2.10}$$

$$\dot\eta_2 = M_4/24 + 5(-M_3\eta_1/6 + M_2\eta_1^2/2 + M_1\eta_2); \tag{2.11}$$

$$\dot\eta_3 = -M_6/720 + 7(M_5\eta_1/120 - M_4\eta_1^2/12 + M_3\eta_1^3/6 - M_3\eta_2/6 + M_2\eta_1\eta_2 + M_1\eta_3); \tag{2.12}$$

$$\dot\eta_4 = +M_8/40320 - M_7\eta_1/560 + 3M_6\eta_1^2/80 - M_5\eta_1^3/4 - \ldots - 3M_3\eta_3/2 + 9M_2\eta_1\eta_3 + 9M_1\eta_4; \tag{2.13}$$

$$\dot{\eta}_5 = -M_{10}/3628800 + 11(M_9\eta_1/362880 - M_8\eta_1^2/10080 + \ldots - M_3\eta_4/6 + M_2\eta_1\eta_4 + M_1\eta_5); \quad (2.14)$$

$$\dot{\eta}_6 = M_{12}/479001600 - 13(M_{11}\eta_1/39916800 + \ldots + M_2\eta_2\eta_4 - M_3\eta_5/6 + M_2\eta_1\eta_5 + M_1\eta_6). \quad (2.15)$$

In what follows, we use, for brevity, the linear combinations of amplitudes

$$M_j = \sum_{m=1}^{N} m^j A_m$$

along with the amplitudes. System (2.4)–(2.15) relates to the case where the order of approximation N of boundary conditions (1.3) is equal to six. Lower-order systems follow from this system when the corresponding high-order equations and the number of unknown functions are reduced.

System (2.4)–(2.15) consists of two subsystems of equations for the unknowns A_n and η_n, respectively. The second subsystem is solvable for the derivatives $\dot{\eta}_n$, whereas the first subsystem (containing the derivatives $\dot{A}_n$) includes the derivatives $\dot{A}_n$ in the form of some linear combinations. The left-hand sides of the equations from the first subsystem can be written in the form

$$\sum_{j=1}^{N} \Gamma_{ij}\dot{A}_j,$$

where the subscript i indicates the equation number, and the $N \times N$ matrix Γ_{ij} has matrix elements that depend only on η_n.

N. A. Inogamov [17] have shown that for $N > 1$ solutions of system (2.4)–(2.15) that are of physical interest are attracted to the hypersurface D imbedded in the space A_n, η_n for which $\det\Gamma_{ij} = 0$. From this follows the hypothesis that these solutions exist in a finite time interval $0 < t < t_c$. An analysis of convergence, whose description is beyond the scope of this paper, has shown that the differences between successive approximations decrease rapidly (near-exponentially) with an increase in N. This indicates good convergence of the results. The moments t_c at which the solution is attracted to D also turned out to be weakly dependent on N.

Note that in the periodic case the perturbed boundary consists of alternating cavities (bubbles) and bulges (jets) of the fluid. Apparently, At $t \to t_c$, series (2.3) diverges. This can indicate that the distance between the singularity that is the closest to the boundary η and the top of the bubble $x = 0, y = \eta_0$ becomes small (see [17]). Let us see how the approach of the singularity influences the results of calculations on a two-dimensional grid.

3. Observation of the Loss of Smoothness. Let us verify the above hypothesis that the smooth evolution of η ends at time t_c because of the formation of a singularity at the top. We first dwell on the question of whether there is some evidence for a disruption in the smooth evolution. A typical numerical example is given in Fig. 1a. Here $A_0 = 0.1$; $\eta_0 = 0$; $\mu = 0.1$; and the fluid over the boundary η is dense. A cavity (bubble) in the dense fluid is located at the left boundary of the computation domain, and a bulge (jet) of this fluid is at the right boundary of the domain. This is the case of Rayleigh–Taylor instability: $g = -1$, the y axis is directed upward. The units are $|g| = 1$ and $k = 1$ (k is the wavenumber). Time is given in the units $1/\sqrt{gk}$. The perturbation with one harmonic is initial. Since the function $\eta(x,t)$ has even symmetry in x, half the period of λ is shown. The rectangular images in the lower row cover the entire computation domain. The height-to-width ratio of this rectangle is 3 : 1 (in Fig. 1 this ratio is retained). To save space, the upper row shows only a part of the rectangle in the form of a band adjacent to the boundary η. At the initial moment, the surface η divides the computation domain in two. For orientation, the corresponding straight line is shown in all images.

The development in time is given in Fig. 1 from left to right and then from top to bottom. This is clearly seen from the perturbation growth. The successive images in Fig. 1 are given in the intervals $t_{n+1} - t_n = 0.5$ from $t = 0$ to $t = 5.5$. The appearance of irregularities M and Q at $t \approx 1.5$ approximately in the middle of the half-period in x is unrelated to the singularity at the top B. This can be due to the fact that $\mu \neq 0$.

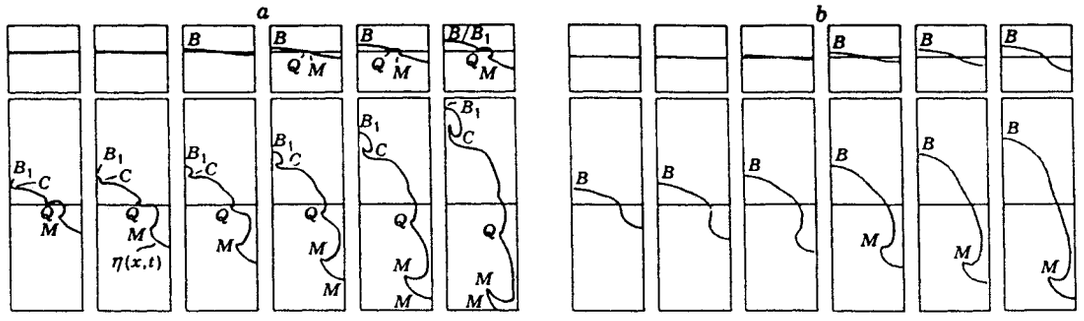

Fig. 1

In any case, the irregularity M gradually becomes the jet $M - M$ (see the last images in Fig. 1a), which forms a "cap" of the mushroom-shaped bluntness. As is known [18], such bluntnesses are associated with the nonzero density ρ_2 of the lower fluid, because the hydrodynamical grid algorithms used do not work for $\mu = 0$. Therefore, to verify the theory, a sufficiently small value of μ was used.

Obviously, the analysis of Fig. 1a provides a positive answer to the question of the loss of smoothness: a singularity approaches the top point of the bubble B at $t_c = 2.5$–3. This can be responsible for the observed appearance of a new, initially small bubble in the vicinity of the top of the old large bubble. The symmetric half of the boundary of the new bubble is given by the arc B_1C. This arc is bounded by the cusp (point) C. The arc B_1C "distends" (inflates) with time. The tops of the bubble at $t < t_c$ and $t > t_c$ are denoted by B and B_1, respectively.

Let us consider the influence of the grid resolution. The dependences on the time Δt and space steps were investigated using grids with both rectangular cells with steps Δx and Δy and square cells with $\Delta x = \Delta y = \Delta$. Accurate calculations with small values of both Δt and Δ turned out to be necessary to obtain satisfactory data. Accordingly, the values of N_{st} and N_{gr} must be large. Here $N_{st} = T/\Delta t$ is the number of time steps, T is the integration time, and $N_{gr} = \lambda/\Delta x$. In particular, the development of the perturbation amplitudes to $\sim\lambda$ requires 10^5–10^6 time steps. The resolution of coarse grids with $\Delta > \lambda/(40$–$50)$ is not enough to reveal singularities — compare the calculations on a coarse grid (Fig. 1b with $\lambda/\Delta = 30$) and on a fine grid (Fig. 1a with $\lambda/\Delta = 110$). This is caused by the decrease in resolution due to the smoothing effect of the grids, which results in smearing the fine details of the picture, and also by an increase in the effective approximation viscosity and the attendant increase in artificial dissipation. As a result, the propagation perturbations is somewhat slowed down (compare the jet locations in the last images of Figs. 1a and 1b). With an increase in Δ, the cusp C, which is formed after moment t_c, is gradually smeared, so that the evolution of η seems to be smooth and without singularities behind some threshold in Δ.

The calculations presented in Fig. 1 were performed by A. V. Chekhlov for $\mu = 0.1$, $A_1(0) = 0.1$, and $A_n(0) = s_n(0) = 0$ by the artificial compressibility method [19]. System (1.1) was integrated. Note that a great number of grid calculations were performed to estimate the degree of reliability of the results. In addition, A. V. Chekhlov used various velocities [$A_1(0) = 0.01$, 0.025, 0.05, 0.1, 0.2, and 0.5], densities ($1/\mu = 2$, 10, 20, and 40), time steps, and $N_{gr} = \lambda/\Delta x$ (20, 40, 60...200, and 220). Moreover, he calculated several variants, in which the perturbation at the initial moment was given by two harmonics A_1 and A_2. The time required to calculate one time step using the method of [20] and a 100×200 grid on a Pentium PC AT-586 processor is ~ 1 sec. The computer time for one variant was $\sim$ 50–100 h.

4. Verification of the Theory by Calculations. Let us study the effect of variation of initial data on the results. We consider variation of the initial amplitude $A_1(0)$. The corresponding variants are presented in Figs. 2 and 3. Figure 2 shows the formation of a singularity at the top of a bubble at small initial amplitudes of perturbation, and Fig. 3 the formation of a singularity at the top at relatively large initial amplitudes. The first two images in the lower row show the early stages of development of the arc B_1C. In these stages, its formation is not yet pronounced. This explains the error in determinating the quantity t_c. Calculations were

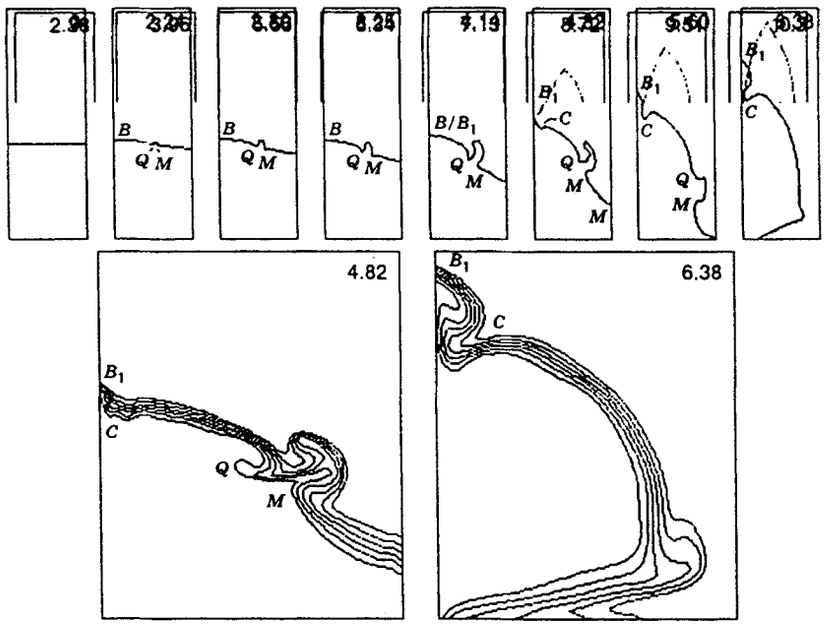

Fig. 2

performed by the method of coarse particles [20] on a grid with $\Delta = \lambda/140$ for $\mu = 0.1$. In this case, the system of gas-dynamic equations (1.2) is integrated. The boundary conditions at the upper and lower boundaries of the computation domain were varied in the calculations. Various rigorous and free boundary conditions were used. Variation of these conditions has shown that they do not influence the observed loss of smoothness. For example, Figs. 1a and 1b refer to the case where free-boundary conditions are specified from above and below, and Figs. 2 and 3 to the case where a free-boundary condition is specified from above and the mass flow vanishes from below. The symmetry conditions were specified at the left and right boundaries.

On the one hand, to obtain high resolution, it is necessary that the parameter λ/Δ be as large as possible. On the other hand, the main-memory size of the computers used limits the maximum grid dimension to ~5000 cells in the method of [19] and ~20,000 cells in the method of [20]. Moreover, the time the processor spent to perform one step in t increases rather quickly with the number of cells (somewhat quicker than in direct proportion to the number of cells), and the step Δt itself decreases proportionally with $1/N_{gr}$ due to the Courant criterion. This leads to the fact that calculations on fine grids are time-consuming because of the limited resources of the processor. Under these conditions, the vertical dimension of the calculation domain should be chosen with caution. Emphasis was given to bubble dynamics. Numerous tests in which the initial depth of the lower low-density fluid was varied have shown that the bubble behavior is strongly independent of the jet behavior. For example, the jet can go through the lower free boundary or collide with it if this is a rigid boundary, turn along it, and then, after colliding with counter jets, rise up inside the bubble (see, for example, Figs. 1a and 2); and this does not have a substantial influence on the fate of the bubble. This independence makes it possible to decrease the vertical dimension of the computation domain at the cost of the lower-fluid depth. In the calculations, whose results are presented in Figs. 2 and 3, the depths of the high- and low-density fluids are in the 7 : 5 ratio at the initial moment (the first image in the upper sequence of Fig. 2).

The calculations shown in Figs. 2 and 3 refer to small and relatively large amplitudes of perturbations, respectively. A singularity at the bubble top forms over the entire range of amplitudes. At $t < t_c$, the shape of the boundary is in satisfactory agreement with that found theoretically. The dependence of the quantity t_c on initial data and its value are also in good agreement with the theoretical data. The shapes of η at $t < t_c$ and the moments t_c calculated by two absolutely different methods [19 and 20] are in satisfactory agreement.

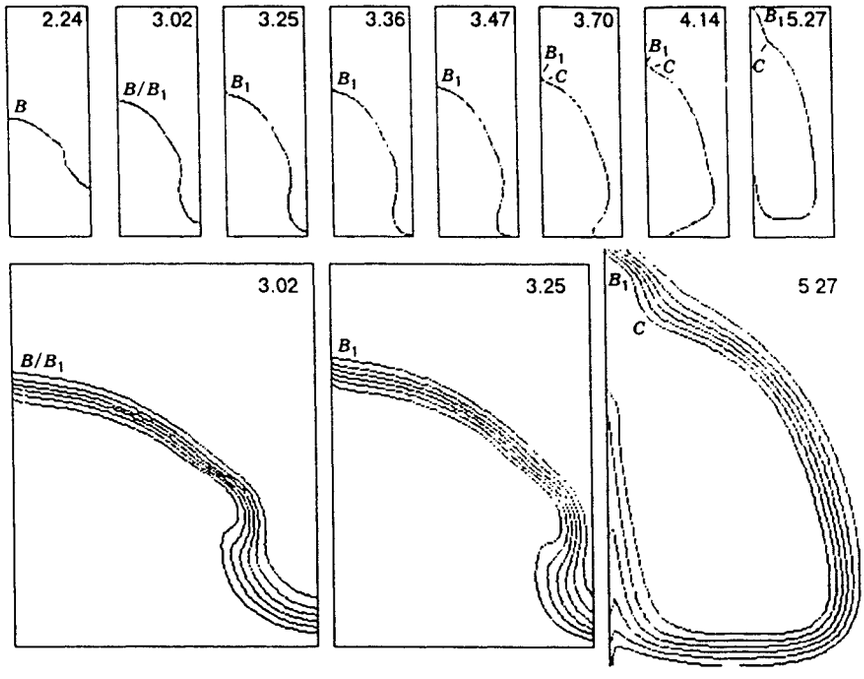

Fig. 3

In Figs. 2 and 3, $A_1(0) = 0.025$ and 0.22, respectively, and the initial velocities differ by an order of magnitude. Therefore, the amplitudes of η perturbations differ markedly at the same moments. In particular, in Fig. 3, the jet reaches the lower boundary earlier, and the top of the bubble reaches the upper boundary earlier than in Fig. 2. This difference is especially noticeable in the early stages (cf. with the images for $t = 2.24$). With an increase in $A_1(0)$, the size of the irregularities M and Q gradually decreases. In Fig. 3, they become unnoticeable. It is possible that, as was proposed in Section 3, they might be related to a mushroom-shaped formation which forms with time at the ends of the jets. Since we were interested in phenomena occurring in the vicinity of the bubble top, the thickness of the low-density fluid layer and, hence, the jet path were reduced and turned out to be small. This does not make it possible to investigate adequately the generation of the mushroom-shaped bluntness. In connection with the question on the dynamics of the boundary area of jets, note that the appearance of a nonanalytical point in this area was predicted for the case where $\mu = 0$ [21, 22]. Whether the corresponding numerical calculations will confirm this prediction based on a weakly nonlinear approximation is still not clear. In addition, it remains unclear whether the condition $\mu = 0$ is important for this problem.

The evolution of the middle isochore $\rho = (\rho_1 + \rho_2)/2$ is shown in Figs. 2 and 3, as in Fig. 1, in the upper sequence of images. The lower row shows the evolution of six neighboring isochores, which divide the density interval between ρ_2 and ρ_1 into six equal sections. These images characterize the degree of smearing of the density profile caused by numerical diffusion when the Euler method is used. The current time is given in the upper right corner. Note that the output data are nonuniform in time. This nonuniformity is caused by the necessity of examining more thoroughly the most important stages of the evolution. In Fig. 3, the output data are most numerous near the moment t_c. The rectangles denote the calculation domain. In Figs. 2 and 3, the upper rectangles are extended in the vertical direction by a factor of 1.68, and the lower rectangles are extended in the horizontal direction by a factor of 1.19. In the lower row of Fig. 2, 20% of the vertical dimension of the domain in the upper part of the rectangle was omitted to reduce the area. The most essential part of the calculation domain is shown at the bottom of Fig. 3.

The calculations are performed over a wide range of initial amplitudes $A_1(0)$, which covers about two orders of magnitude. The theoretical and numerical functions $t_c(A_1(0))$ are presented in Table 1. Evidently, if

TABLE 1

$A_1(0)$	t_c	
	Theory	Calculation
0.01	5 ± 0.5	4.5 ± 0.5
0.025	4.3 ± 0.5	4.3 ± 0.5
0.05	3.6 ± 0.5	3.2 ± 0.5
0.1	2.9 ± 0.5	2.7 ± 0.5
0.22	2.3 ± 0.5	3.0 ± 0.2
0.34	1.7 ± 0.5	2.9 ± 0.5
0.70	1.4 ± 0.5	2.7 ± 0.5

the discrepancy for relatively high amplitudes, which somewhat exceeds the error, is ignored, one can conclude that these functions are in satisfactory agreement. The theoretical value of t_c was determined by two methods. According to the first method, the time at which det t_c decreases by a factor of 1000 compared with the initial value was taken as det Γ. The error in this case is determined by the spread in the values of t_c with variation of N. In the second method, a norm that determines the distance between trajectories was introduced. The moment at which this norm exceeds some given number was taken as t_c. The error was determined by a reasonable variation of this number and N. Table 1 gives the total error of these methods. This numerical error is due to the difficulty in determining t_c. The fact is that the bubble B_1C is not pronounced in the vicinity of t_c. This is evident in the upper sequence of images in Fig. 3 in the time range of $3.02 < t < 3.7$ (see also the enlarged images in the lower sequence at $t = 3.02$ and 3.25).

Mention should be made of some difficulties arising in the calculation of extreme variants with low or high initial velocities. The number of integration steps N_{st} increases at the boundaries of the velocity range given in Table 1. This complicates calculations outside this velocity range. We shall explain the causes of the growth of N_{st}. The small values of $A_1(0)$ were calculated for $g = 1$. The step Δt that is chosen as some fraction of the inverse increment $1/\gamma$ ($\gamma = \sqrt{gk}$) or by the Courant criterion is fixed. Its determination in accordance with the Courant criterion is due to the fact that the sound velocity is higher than the hydrodynamic velocity and does not vary, whereas the integration time T increases with a decrease in $A_1(0)$. This explains why N_{st} grows at low velocities. At high velocities, N_{st} increases, because $A_1(0)$ was fixed, and g was decreased in the numerical calculations. The final data in all the figures and Table 1 are presented in units $g = k = 1$. If Δt and $A_1(0)$ are fixed, and g decreases, then N_{st} increases, because a decrease in g leads to slowing down the development process. Note also that for very small $A_1(0)$ (< 0.01) small-scale perturbations appear throughout the boundary η at time $t < t_c$. Their appearance is probably due to grid-generated perturbations. As a result, it is impossible to determine t_c numerically.

5. Evolution of the Solution After Contact with a Singularity. The situation at $0 < t < t_c$ and $t \approx t_c$ was analyzed above. Grids with maximum possible values of N_{gr} were used to investigate this situation in detail. Due to the limited memory, this led to a small height of the calculation domain. For example, in the calculations presented in Figs. 2 and 3, the ratio of the path D_b the bubble top could travel to the period λ was 0.5. The quantity D_b is equal to the thickness of the dense-fluid layer. To minimize the boundary effect, free boundary conditions were usually specified from above. Due to the relatively small ratio D_b/λ, the bubble B_1C approaches the upper boundary soon after time t_c. In so doing, the bubble still remains small. This means that not much time has passed after the contact with the singularity.

Let us consider the solution of the problem for moments when the cusp C moves to great distances ($\sim \lambda/2$ and more) from the top B_1. For this, the ratio D_b/λ must be increased. Since the total number of cells is limited by the memory, N_{gr} must be decreased. Fortunately, this turned out to be possible. The wavelength can be halved relative to the horizontal grid size and, correspondingly, the path of the bubble top can be doubled. The parameter Δ/λ still remains small enough to resolve the appearance of a singularity.

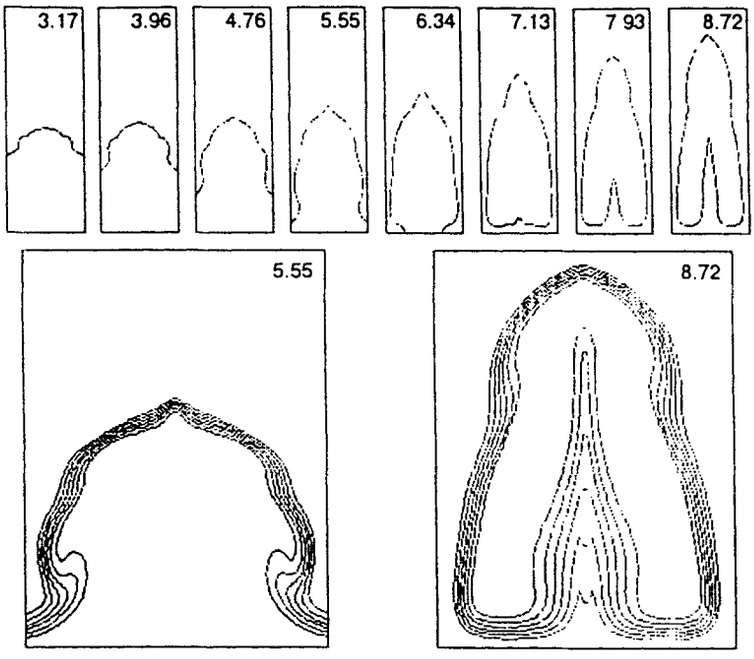

Fig. 4

Examples of such calculations are shown in Figs. 4 and 5, where the grid is 70×120, $\Delta = \lambda/70$ (this step is sufficient to reveal the contact with the singularity), and $D_b/\lambda = 1$. The time step in the units $g = k = 1$ was $\approx 7 \cdot 10^{-5}$. Figures 4 and 5 give the rapid and slow variants of perturbation development. Here the initial amplitude equals $A_1(0) = 0.079$ and 0.023, respectively. In Fig. 4, the contact with the singularity takes place at $t_c = 4.1 \pm 0.3$. This value is somewhat larger than that obtained in integration with the doubled quantity N_{gr}. A small subharmonic perturbation with doubled wavelength and with initial velocity amplitude $A_{0.5} = 0.0039$ and $A_{0.5}/A_1 = 1/6$ was superimposed on the basic velocity perturbation to see how the symmetry breakdown influences the formation of a singularity. As is seen, if the amplitude $A_1(0)$ is smaller, the contact occurs later at $t_c = 4.6 \pm 0.3$, as it must be. Because of the initial asymmetry, the entire solution is asymmetric.

Let us examine the structure of the solution when the arc length is $B_1C \sim \lambda/2$. This condition is satisfied in the final images of the sequence presented in Figs. 4 and 5. The formation of wedge-shaped tops on the surface η is the most striking feature. Measurements of the wedge angle give values close to 120°. In checking these measurements, the reader should take into account the distortion coefficient of the ratio of vertical to horizontal dimensions (see Section 4).

The formation of a wedge-shaped top in the asymmetric case in which the basic solution is perturbed by a small subharmonic is shown in Fig. 5. Again, as in the symmetric case, the angular measurements give values close to 120°. The full calculation domain is shown in the upper and lower rows in Figs. 4 and 5. The top must form immediately after moment t_c. Some evidence for such tops is also given in Figs. 2 and 3. The wedge angle α changes with time (somewhat increases) in the early stages at t_c. After a great period of time from the moment t_c, the quantity α presumably reaches an asymptotic value. Measurements in the early stages are difficult, because the arc B_1C is small. Measurements of the angle α as a function of $(t - t_c)$ for $(t - t_c) \ll t_c$ require accurate calculations on fine grids. Measurements in the later stages give $\alpha = 115° \pm 10°$, i.e., the angle is approximately equal to 120°.

In the later stages, i.e., at $t \gg t_c$, a steady-state solution must be gradually reached. This solution is stationary in a moving coordinate system related to the boundary η. An exact steady-state solution exists in the incompressible case, when the Mach number is $M = 0$, and under the conditions $\mu = 0$ and $g = 1$. For $M \ll 1$ and $\mu \ll 1$, a quasi-steady-state stage appears instead of an exact steady state. This stage exists

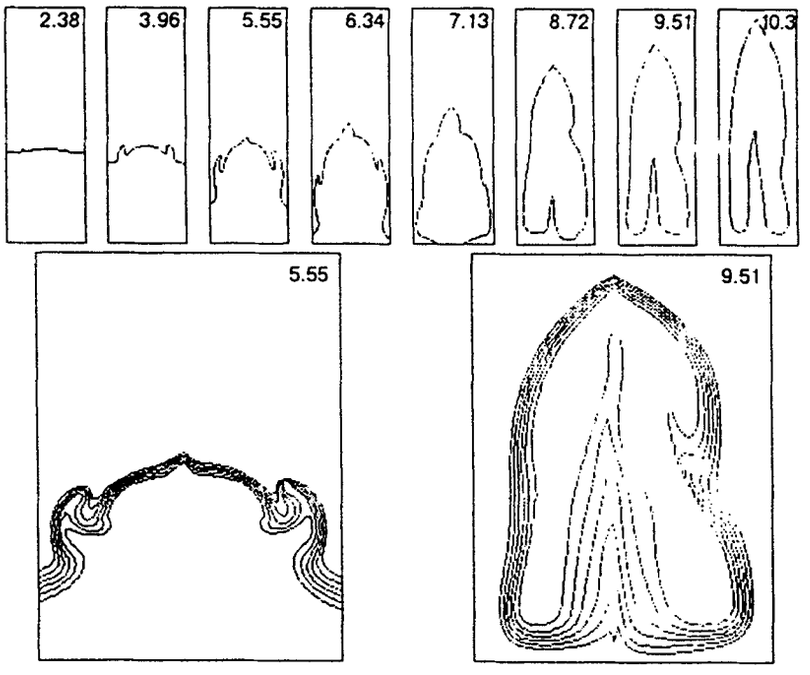

Fig. 5

for a long time owing to the smallness of M and μ. The asymptotic solutions for $g = 0$ requires a separate consideration. Note that there are no repeat contacts with singularities in the vicinity of the bubble top.

We give two types of a simple steady-state solution that satisfies boundary conditions (1.3):

$$f_1 = 2\sqrt{(1-\mu)g}\exp(i\pi/4)\,z^{3/2}/3, \quad f_2 = 2\sqrt{(1-\mu)g}\exp(-i3\pi/4)\,z^{3/2}/3. \tag{5.1}$$

Here $f = \varphi + i\psi$ is the complex potential, and $z = x + iy$. The solution f_1 can be shown to correspond to a solitary bubble filled with a fluid at rest with density ratio μ. The free surface η of the bubble forms a wedge for $\alpha = 120°$. The solution f_2 corresponds to a solitary wave with an infinite amplitude at the interface between the moving fluid and the fluid at rest with density ratio μ. As is known, the solution f_2 describes the asymptotic flow behavior in the vicinity of the wedge-shaped top of a crest with an angle of 120° of the limiting Stokes wave. Obviously, the solution f_1 relates to the asymptotic flow behavior in the vicinity of the bubble top, which gradually reaches a steady-state value at $t > t_c$. It seems likely that precisely this solution behavior is observed in Figs. 2–5. A detailed investigation of the steady-state solution requires large values of the parameter D_b/λ and, hence, large grids and long calculations.

Note that in the calculations by the method of [19], at $t > t_c$ bubbles with rounded-off tops are obtained (Fig. 1a). Nevertheless, the solutions with wedge-shaped tops calculated by the well-known method of coarse particles [20] should be viewed seriously. The fact is that it is easy to imagine how a numerical algorithm could "gloss over" smooth a wedge-shaped top due to the influence of artificial viscosity or insufficient resolution. But it is difficult to imagine how a numerical method could "artificially" cause first the formation and then the steady existence of such a top.

6. Conclusions. Analysis was made of the solutions of the equations of continuum mechanics, which describes the motion of an incompressible fluid or a weakly compressible gas separated by a contact boundary into regions with different densities. We put forward the hypothesis that a singularity approaches this boundary and attaches to it. The contact with the singularity divides the evolution into two stages. The approach and the contact with this singularity takes place in the first stage. The system with the attached singularity further evolves and the second stage starts. The solution in the second stage was investigated in detail. No repeat contacts with singularities occur under the periodic boundary conditions. Moreover, we proposed the

hypothesis that after moment t_c the solution has a wedge-shaped top at the contact boundary. This hypothesis is based on numerical results and on the fact that an exact solution that corresponds to a solitary wedge-shaped bubble with an apex angle of 120° exists in the hydrodynamics of heavy fluids. Some time after moment t_c, the apex angle at this top is approximately equal to 120°.

The authors express their gratitude to S. I. Anisimov and A. M. Zhilyayev for helpful discussions, and to A. V. Chekhlov for his help in the calculations.

This work was supported by the Russian Foundation for Fundamental Research (Grant 95-02-06381-a). N. A. Inogamov is also grateful to INTAS-94-1105, the International Scientific Foundation, and the Government of the Russian Federation.

REFERENCES

1. H. Lamb, *Hydrodynamics* [Russian translation], Gostekhteoretizdat, Moscow–Leningrad (1947).
2. M. I. Gurevich, *Theory of Jets of an Ideal Fluid* [in Russian], Fizmatgiz, Moscow (1961).
3. L. N. Sretenskii, *Theory of Wave Motions of a Fluid* [in Russian], Nauka, Moscow (1977).
4. L. V. Ovsyannikov, "Asymptotic representation of solitary waves," *Dokl. Akad. Nauk SSSR*, **318**, No. 3, 556–559 (1991).
5. R. D. Richtmyer, "Taylor instability in shock acceleration of compressible fluids," *Commun. Pure Appl. Math.*, **13**, 297–319 (1960).
6. E. E. Meshkov, "Instability of the interface between two gases accelerated by a density discontinuity," *Izv. Akad. Nauk SSSR, Mekh. Zhidk. Gaza*, No. 5, 151–155 (1969).
7. V. B. Rosanov, I. G. Lebo, S. G. Zaitsev, et al., "Experimental investigation of gravitational instability and turbulent mixing of stratified flows in the field of acceleration for the problems of inertial thermonuclear synthesis," Preprint, Physical Inst., Acad. of Sciences, Moscow (1990).
8. R. Benjamin, D. Besnard, and J.-F. Haas, "Richtmyer–Meshkov instability of shocked-gaseous interfaces," in: *Shock Waves*: Proc. of the 18th ISSWST, Sendai, Japan, 1991, Springer-Verlag, Berlin (1992).
9. D. L. Youngs, "Numerical simulation of turbulent mixing by Rayleigh–Taylor instability," *Physica D, Nonlinear Phenomena*, **12D**, 32–44 (1984).
10. Yu. A. Kucherenko, G. G. Tomashev, and L. I. Shibarshov, "Experimental investigation of gravitational turbulent mixing in a self-simulating regime," in: *Questions of Atomic Science and Engineering, Ser. Theoretical and Applied Physics*, No. 1 (1988), pp. 13–19.
11. N. N. Anuchina, M. G. Anuchin, V. I. Volkov, et al., "Numerical investigation of the effect of compressibility of a medium on the development of Rayleigh–Taylor instability," in: *Questions of Atomic Science and Engineering, Ser. Simulation of Physical Processes*, No. 2 (1990), pp. 10–16.
12. V. V. Nikiforov, "Turbulent mixing at the contact boundary between media with different densities," in: *Questions of Atomic Science and Engineering, Ser. Theoretical and Applied Physics*, No. 1 (1985), pp. 3–12.
13. E. G. Gamaly, A. P. Favorsky, A. O. Fedyanin, et al., "Nonlinear stage in the development of hydrodynamic instability in laser targets," *Laser Part. Beam.*, **8**, 399–407 (1990).
14. V. E. Neuvazhayev and V. G. Yakovlev, "A model and method of numerical calculation of turbulent mixing of an interface moving with acceleration," in: *Questions of Atomic Science and Engineering, Ser. Techniques and Programs for Numerical solution of Problems in Mathematical Physics*, No. 2 (1984), pp. 16–20.
15. S. W. Haan, "Weakly nonlinear hydrodynamic instabilities in inertial fusion," *Phys. Fluids B*, **3**, 1992–2000 (1990).
16. P. R. Garabedian, "On steady-state bubbles generated by Taylor instability," *Proc. Roy. Soc. London Ser. A*, **241**, 423–431 (1957).
17. N. A. Inogamov, "Singular mixing in stars," *Pis'ma Astron. Zh.*, **20**, No. 10, 754–761 (1994).

18. S. I. Anisimov, A. V. Chekhlov, A. Yu. Dem'yanov, and N. A. Inogamov, "The theory of Rayleigh–Taylor instability: modulatory perturbations and mushroom-flow dynamics," *Russian J. Comp. Mech.*, **1**, No. 2, 5–32 (1993).
19. N. A. Inogamov, A. V. Chekhlov, "Existence, uniqueness and physical selection of asymptotically steady-state solutions in the theory of Rayleigh–Taylor instability," in: *Proc. of the 4th Int. Workshop on the Phys. of Compressible Turbulent Mixing*, P. F. Linden, D. L. Youngs, and S. B. Dalziel (eds.), Cambridge Univ. Press (1993), pp. 50–56.
20. O. M. Belotserkovskii and Yu. M. Davydov, *The Method of Coarse Particles in Gas Dynamics* [in Russian], Nauka, Moscow (1982).
21. E. A. Kuznetsov, M. D. Spector, and V. E. Zakharov, "Surface singularities of an ideal fluid," *Phys. Lett. A*, **182**, 387–393 (1993).
22. E. A. Kuznetsov, M. D. Spector, and V. E. Zakharov, "Formation of singularities on the free surface of an ideal fluid," *Phys. Rev. E*, **49**, 1283–1290 (1994).